THE ASTRONOMICAL JOURNAL VOLUME 89, NUMBER 10 OCTOBER 1984

STRUCTURE OF THE URANIAN RINGS. I. SQUARE-WELL MODEL AND PARTICLE-SIZE CONSTRAINTS

J. L. ELLIOT[a)]
Department of Earth, Atmospheric, and Planetary Sciences and Department of Physics, Massachusetts Institute of Technology, Cambridge, Massachusetts 02139

R. G. FRENCH
Department of Earth, Atmospheric, and Planetary Sciences, Massachusetts Institute of Technology, Cambridge, Massachusetts 02139 and Department of Astronomy, Wellesley College, Wellesley, Massachusetts 02181

K. J. MEECH [a)]
Department of Earth, Atmospheric, and Planetary Sciences, Massachusetts Institute of Technology, Cambridge, Massachusetts 02139

J. H. ELIAS
Department of Physics, California Institute of Technology, Pasadena, California 91125
Received 20 March 1984; revised 3 July 1984

ABSTRACT

A square-well model for occultation profiles produced by the Uranian rings is described. The model includes diffraction effects and treats the occulting ring segment as a uniformly transmitting gray screen with abrupt edges. Up to ten parameters of the model can be fit by least squares to a ring profile; those describing the profiles of the ring are: (i) the midtime of the profile, which specifies the position of the occulting ring segment; (ii) the duration of the ring occultation, which is proportional to the radial width of the ring; and (iii) the fractional transmission of the ring, which is simply related to its optical depth. The diameter of the occulted star can also be fit as a free parameter. For our data with the highest signal-to-noise ratio, we can achieve a precision of tens of meters in the placement of a ring segment, a precision of one-hundred meters in the width of a segment, and a precision of a few hundredths in its fractional transmission. This model has been used to fit occultation profiles obtained simultaneously at more than one wavelength in order to constrain the distribution of particle sizes within the rings. We analyzed the 10 March 1977 observations that were made from the Kuiper Airborne Observatory at 0.619, 0.728, and 0.852 μm and the 22 April 1982 observations that were made from Cerro Tololo at 0.88 and 2.2 μm. Within the precision of the data, no wavelength dependence of the optical depth was found. This result can be explained if less than 10% of the optical depth at these wavelengths is contributed by submicron-sized particles. This constraint is compared to limits placed on particle distributions by the spectrum and phase function of the rings. To obtain data most amenable to the profile fitting analysis described here, observers of future Uranian ring occultations should, if possible, record their data unchopped, and obtain the signal level from the unocculted star immediately following each ring occultation.

I. INTRODUCTION

According to our present picture, the Uranian ring system consists of nine sharp-edged ringlets, several of which are narrower than the 4-km resolution limit of Earth-based occultation observations (Elliot and Nicholson 1984). The ring particles follow inclined, eccentric ellipses that precess due to the harmonics of the Uranian gravitational potential (French *et al.* 1982). Since particle collisions would broaden a narrow ring in a time much less than the age of the solar system (Goldreich and Tremaine 1982), either the rings formed recently or external forces have prevented the particles from spreading. Lacking specific evidence for recent formation and not seeing any rings that are in the process of spreading apart, most assume that narrow ringlets are confined by the external forces produced by nearby satellites (Goldreich and Tremaine 1979, 1982). The Voyager discovery of two satellites "shepherding" Saturn's F ring strongly supports the model for this ring; however, observations to date have not revealed the postulated shepherds for other Saturnian ringlets (Smith *et al.* 1982).

Uranian ring shepherds, if they exist, would perturb the ring orbits in two ways: First, a shepherd would cause its ring to precess faster than the rate forced by the oblateness of Uranus alone; second, a shepherd would excite particle oscillations in the radial direction. The magnitudes of these effects, which depend on the mass of the shepherd and its distance from the ring, appear comparable to the precision presently attained with the orbit model based on occultation timings (French *et al.* 1982; Freedman *et al.* 1983). Other information bearing on the strength of the shepherd mechanism, as well as other possible gravitational confinement mechanisms for the narrow rings, would be the distribution of particle sizes within the rings. From investigations of the spectrum and phase function of the rings, Pang and Nicholson (1984) have concluded that the majority of Uranian ring particles lie within the size range 0.1–10 μm.

Constraints on the particle sizes can also be obtained by comparing the optical depths of ring occultation profiles recorded at different wavelengths, as has been done with Voyager radio and ultraviolet occultation data for Saturn's rings (Tyler *et al.* 1983; Marouf *et al.* 1983; Esposito *et al.* 1983). For the Uranian rings, we can investigate the ~ 1 μm particle population by comparing infrared and optical occultation profiles.

[a)] Visiting Astronomer, Cerro Tololo Inter-American Observatory, La Serena, Chile, which is supported by the National Science Foundation.

 0004-6256/84/101587-17$00.90

The investigation of possible orbit perturbations by shepherd satellites and the establishment of constraints on the particle sizes requires an extensive analysis of the occultation profiles of the rings. We must obtain their widths, optical depths, and midtimes—along with rigorous errors in these quantities. Previous work has developed a square-well diffraction model for the rings (Nicoholson *et al.* 1978, 1982; Elliot *et al.* 1981); while not perfect, it is a good first approximation, at least providing a standard of comparison for ring structure. In this paper, we shall: (i) extend the diffraction model analysis to include least-squares fitting, so that we can determine errors in the parameters describing the ring structure, and (ii) use this model to determine the relative optical depths of the rings at visible and near-infrared wavelengths. In Paper II of this series (French *et al.* 1984), we shall investigate the widths of the rings as a function of orbital longitude, in order to improve the width-radius relations of the rings (Elliot and Nicholson 1984). A later product of these investigations will be angular diameters for the occulted stars.

II. MODEL

We consider a perfectly flat, elliptical ring and define its width W at any orbital longitude to be the distance between its inner and outer edges, measured along the radius vector originating from the focus of its orbit ellipse that coincides with the center of motion (see Fig. 1). In our model, the fraction of light transmitted by the ring is constant along a radius vector; hence, the transmission versus orbital radius would be a "square well." We assume that any variation of the fractional transmission with orbital longitude occurs on scales greater than a few kilometers, so that the transmission of the ring would be constant over the longitude range sampled by a single occultation profile. The finite longitude interval sampled depends on the size of the Fresnel scale and the angle between the apparent path of the star and the radius vector from the center of motion to the ring segment.

Viewed at an angle B_k from the plane of the k th ring, the observer would measure a fractional transmission f_0 which is related to the optical depth of the ring τ_0 by

$$f_0 = e^{-\tau_0} . \tag{1}$$

If the ring is many particles thick (polylayer), then the optical depth normal to the ring τ_n would be related to the observed value by

$$\tau_n = \tau_0 \sin B_k \quad \text{(polylayer)} . \tag{2}$$

However, if the particles in the ring formed a monolayer, then for values of B_k larger than those for which significant shadowing occurs, we would have the following relation between the fractional transmission normal to the ring f_n and the fractional transmission that would be observed at an angle B_k:

$$(1 - f_n) = (1 - f_0) \sin B_k \quad \text{(monolayer, no shadowing)} . \tag{3}$$

If diffraction effects are neglected for the moment, the occultation profile of a model ring would be a square well of fractional transmission f_0 and duration T_0, centered at a time t_0. From these observed quantities, we would obtain the width in the ring plane from the relation

$$W = v_r T_0 , \tag{4}$$

where v_r is the apparent radial velocity of the occulted star in the plane of the ring.

In view of the simple transformation given by Eq. (2), we see that optical depth would be most useful to express the transmission of a polylayer ring. Similarly, the transmission of a monolayer ring would be most usefully expressed as its fractional transmission [see Eq. (3)]. We now define two other ways to express the ring transmission, closely related to the two just discussed. The first is the product of the fraction of the light absorbed and/or scattered by the ring and the width of the ring, which we term the "equivalent width." It is useful to define this in units of both length and time:

$$\begin{aligned} E &= W(1 - f_0) \sin B_k \quad \text{(length)} , \\ E_0 &= T_0(1 - f_0) \quad \text{(time)} . \end{aligned} \tag{5}$$

For a monolayer ring, E would not vary with B_k, since $(1 - f_0) \sin B_k$ would be constant [Eq. (3)].

The second quantity that we have found useful for fitting ring profiles is the "equivalent depth," which we denote by A and define:

$$\begin{aligned} A &= W\tau_0 \sin B_k \quad \text{(length)} , \\ A_0 &= T_0\tau_0 \quad \text{(time)} . \end{aligned} \tag{6}$$

For a polylayer, A is a direct measure of the abundance of ring material, and is independent of the viewing geometry implied by B_k [Eq. (4)].

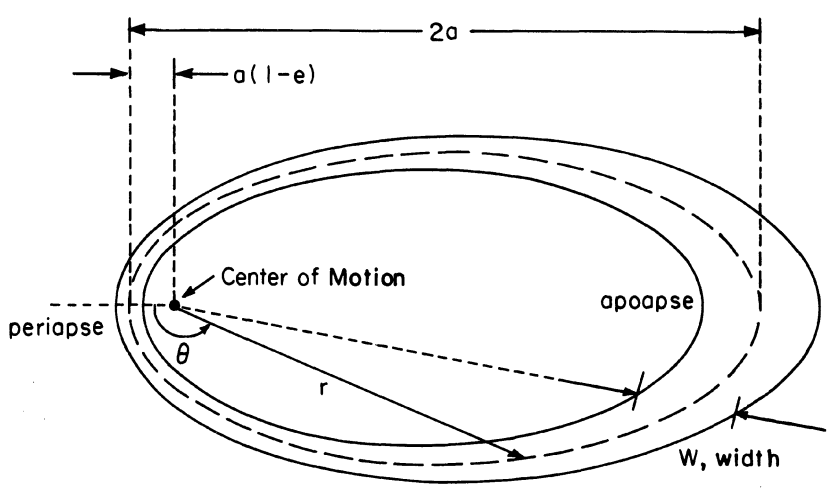

FIG. 1. Ring geometry (exaggerated view). This diagram shows the plane of an infinitely thin ring, whose width varies with orbital longitude θ. The particle orbits within the ring are assumed not to cross, and the (mean) orbit of the ring is defined as the ellipse traced by the midpoint of the ring. The width of the ring W is the distance, along a radius vector from the center of motion, between the inner and outer edges of the ring.

The diffracted occultation profile for a point source has been calculated in the Appendix in terms of t_0, f_0, T_0, the square-well parameters (see Fig. 2); $v_\perp$, the apparent velocity (in the sky plane) of the star perpendicular to the edge of the ring; D, the distance from the observer to the ring; and λ, the wavelength of the light. We denote the occultation profile of a point source by $P(t, t_0, f_0, T_0, v_\perp, D, \lambda)$, which is a function of time and the parameters defined above. The product of this profile and a function $F(\lambda)$ that gives the relative level of the recorded signal from the star versus wavelength must be integrated over wavelength:

$$\overline{P}(t) = \int_0^\infty F(\lambda) P(t, t_0, f_0, T_0, v_\perp, D, \lambda) d\lambda . \tag{7}$$

To reduce the complexity of the notation, we have dropped the explicit functional dependence of $\overline{P}(t)$ on t_0, f_0, T_0, $v_\perp$, D, and λ.

The diffracted profile must be convolved with the strip-brightness distribution of the occulted star, $s(t)$. If θ_* is the angular diameter of the star, and b is a parameter describing the limb darkening ($b = 0$ for a uniform disk and $b = 1$ for a fully darkened disk), then we define $T_* = D\theta_*/v_\perp$, and $s(t)$ is given by (Elliot *et al.* 1976):

$$s(t) = \frac{4(1-b)\mu + b\pi\mu^2}{2\pi(1-b/3)} , \tag{8}$$

where

$$\mu = [1 - (2t/T_*)^2]^{1/2} \quad \text{for } |t| \leqslant T_*/2$$
$$\mu = 0 \quad \text{for } |t| > T_*/2 .$$

The point-source model must also be convolved with the impulse response of the signal detection and recording system. For the optical data, the impulse response is well approximated by a delta function for time scales of interest. However, for most infrared observations, the appropriate impulse response $h(t)$ is given by

$$h(t) = \left(\frac{t}{t_c^2}\right) e^{-t/t_c} \quad \text{for } t \geqslant 0$$
$$h(t) = 0 \quad \text{for } t < 0 , \tag{9}$$

where t_c is the time constant. We define $c(t)$ as the convolution of $s(t)$ and $h(t)$:

$$c(t) = \int_{-\infty}^{T_*/2} s(t') h(t - t') dt' . \tag{10}$$

If the signal level from the unocculted star is $\bar{n}_*$, then the signal from the star as a function of time $n_*(t)$ is given by

$$n_*(t) = \bar{n}_* \int_{-\infty}^{t + T_*/2} c(t - t') P(t') dt' . \tag{11}$$

A precise description of the slope of the full-scale signal level depends on its source of origin. For example, if the slope were due solely to a drift in the transparency of the atmosphere, then it should be expressed as a time dependence in $n_*(t)$ and convolved with $h(t)$, but not $s(t)$. Here we have assumed that any drift is due to a term added to the background after convolution with $h(t)$ and has a linear slope $\dot{n}_b$. We define the background signal by $n_b(t)$, which has a value $\bar{n}_b$ at time t_0:

$$n_b(t) = \bar{n}_b + \dot{n}_b(t - t_0) . \tag{12}$$

The data are recorded as a series of mean values, averaged over an integration time Δt. In terms of quantities defined above, the model value for the recorded signal for the ith integration bin $n(t_i)$ would be given by

$$n(t_i) = \frac{1}{\Delta t} \int_{t_i - \Delta t/2}^{t_i + \Delta t/2} [n_b(t) + n_*(t)] dt . \tag{13}$$

Within the framework of the square-well model for the ring transmission, Eq. (13) describes the expected signal for a ring-occultation profile in terms of the weighting function

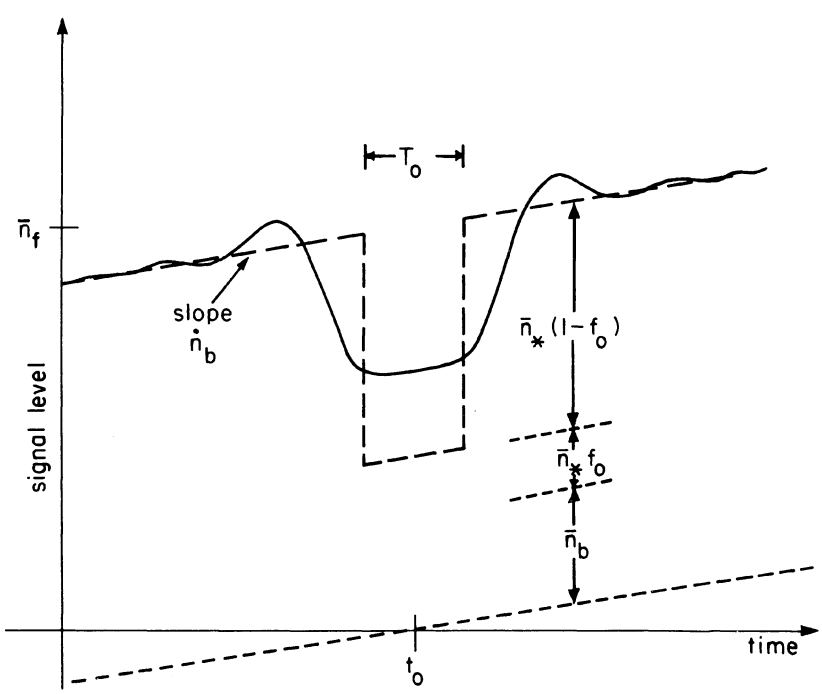

FIG. 2. Model occultation curve. Our model ring transmits a constant fraction f_0 of the incident starlight $\bar{n}_*$ through any point between its inner and outer edges. A background signal with a slope $\dot{n}_b$ and mean value $\bar{n}_b$ at the mid-time of the ring occultation has been added to the signal, and the result is shown by the dashed line. When diffraction is included and the profile is convolved with a fully darkened stellar disk having the same angular diameter as subtended by the ring, the resulting model curve is shown by the solid line.

$F(\lambda)$ and several parameters. These are summarized in Table I.

III. CALCULATION PROCEDURES

Several practical issues arise in implementing Eq. (13) to calculate model occultation profiles and in using least-squares fitting to compare the model signal $n(t_i)$ with the recorded data $N(t_i)$. One class of problems is concerned with calculating the model function to sufficient accuracy—we strive for 0.1%—without requiring an excessive amount of computing time. Our general procedure here is to use a finer and finer mesh to calculate the three integrals in Eq. (13) until the model converges to our required accuracy. When fitting the model, we also verify that a finer mesh does not result in significant changes in each fitted parameter (greater than 0.1 of its formal error). Faster convergence is achieved by using the integrals of the functions $s(t)$ and $h(t)$ over the mesh interval and then normalizing the mesh points for $c(t)$ so that their sum is exactly 1.00 before convolving with $\overline{P}(t)$. Due to the convolution, $\overline{P}(t)$ must be calculated for intervals before and after the actual data interval. The most important error introduced by the necessity of neglecting the infinite tail of $h(t)$ is a systematic shift in the midtime of the profile. For the form of $h(t)$ given by Eq. (9), the systematic shift in the midtime of a profile would be about $2t_c$ if the convolution integral could be calculated over an infinite interval. If the convolution is done with $h(t)$ defined over a finite interval T, a systematic error of about $-t_c(t_c/T)^2$ is introduced into t_0, the fitted midtime. In practice, we insure that T is large enough that the systematic error is much smaller than the formal error in t_0.

The next computational issues arise in the least-squares fitting procedure. Our computer code has been written with the capability of fitting ten model parameters. In describing the ring transmission, we can fit for either the fractional transmission, the equivalent width, or the equivalent depth. The actual model profile is the same, no matter which of the three alternatives is used. The main practical difference is that in some cases the equivalent width has lower correlations with the other parameters, so that the fitting procedure converges more rapidly for the noisier data. The lower correlations also mean that the equivalent width can be fitted with a lower formal error. Also, we actually fit for the full-scale signal level, $\bar{n}_f = \bar{n}_b + \bar{n}_*$, the sum of the mean background and star signals, since it is a more stable parameter to fit. For data so noisy that a ring occultation is just recognizable, we can fit for the full signal level, the background slope, the equivalent width of the ring, and the midtime of the ring occultation. In such a fit, the ring width can also be included as a free parameter, but will have too large a formal error to be useful. The other parameters would be fixed at values determined from other information.

For data of high signal-to-noise ratio, more parameters can be fit. For profiles with visible diffraction fringes, the sensitivity of the fringe amplitude to the ring transmission makes it possible to obtain reliable values for the ring transmission, as well as the star signal level. The most difficult parameter to fit has proven to be the limb-darkening parameter for the occulted star.

One of the hazards of nonlinear least-squares fitting is getting erroneous results by finding a local minimum in the sum of squared residuals, rather than a global minimum. This can occur when the model function is not well approxi-

TABLE I. Model occultation profile parameters.

Signal Levels	
$\bar{n}_b$	Background Average (counts s^{-1})
$\dot{n}_b$	Background Slope (counts s^{-2})
$\bar{n}_*$	Unocculted Star Level (s^{-1})
$\bar{n}_f$	Full Scale ($\bar{n}_b + \bar{n}_*$) (counts s^{-1})
Ring Properties and Event Geometry	
t_o	Midtime (s)
T_o	Duration (s)
f_o	Fractional Transmission
E_o	Equivalent Width (s)
A_o	Equivalent Depth (s)
$v_\perp$	Perpendicular Velocity (km s^{-1})
Convolution Parameters	
T_*	Star Diameter (s)
b	Limb Darkening Parameter
t_c	Time Constant (s)

mated by the linear terms in the Taylor series expansion over a range corresponding to the formal error in each parameter.

The last issue to consider concerning our calculation procedures is the noise statistics of the data. For optical data with photon noise as the dominant factor, the impulse response of the data recording system is a delta function. Since this is white noise, the formal errors in the fitted parameters should be realistic uncertainties in the parameters—if our model is correct. However, when the data recording electronics involves an impulse response such as given in Eq. (9), the noise in neighboring data points becomes correlated. The correct least-squares procedure for fitting a model to data containing correlated noise requires additional matrix multiplications that would make our problem computationally prohibitive (Clifford 1973). The alternative is to deconvolve the impulse response from the data. For some data sets, the chopping signal can not be completely removed by the deconvolution procedure, and the noise is difficult to estimate reliably. Our usual procedure is to fit our model to the deconvolved data, rather than to the raw observations. To determine the noise properties of the deconvolved data, we deconvolve a portion of the occultation which has a roughly constant signal level. (This is typically a section just prior to, or just after, a ring event.) If the power spectrum of the processed observations is flat, as expected for white noise, then the formal errors of the fit are probably accurate. However, if the power spectrum contains strong, distinct features near the chopping frequency or its harmonics, then the formal errors may be unreliable, and other methods must be used to estimate the errors.

As a practical example to illustrate our fitting procedures, we consider the emersion profile for ring 4, shown in Fig. 3, obtained from the South African Astronomical Observatory (SAAO) on 25 March 1983 (Elliot *et al.* 1984). Each data point represents a 0.1-s integration. This profile has large diffraction fringes and a high signal-to-noise ratio. We performed five sample model fits to this profile. For Fits #1, #2, and #3, the perpendicular velocity $v_\perp$ was fixed at the value determined from known ring geometry, based on the ring-orbit model of French *et al.* (1982), and the star level $\bar{n}_*$ was fixed at its photometrically determined value. The time constant of the electronics was much smaller than the data sampling interval, and was set to zero, and the limb-darkening parameter b was set to 1.0, corresponding to a fully darkened disk. These three fits differ only in the free parameter used to measure the transmission: fractional transmission for Fit #1, equivalent width for Fit #2, and equivalent depth for Fit #3. Fit #4 is similar to Fit #1, except that $v_\perp$ and $\bar{n}_*$ were allowed to be free parameters. In Fit #5, the ring was forced to be totally opaque ($f_0 = 0$). The results are given in Table II, and correlation coefficients for Fits #1–#4 are given in Table III. If the limb-darkening parameter is fit also, we get a value for b that has a very large error [$\sigma(b) = 19.1$].

Several conclusions can be reached from these results. Comparing the rms residuals for Fits #4 and #5 in Table II, we see that the model allowing the ring transmission to vary achieves a better fit than our model with the ring transmission factor set to zero. The fitted star diameter agrees well with that calculated from the lunar occultation data of Ridgway *et al.* (1980), although the occulted star has an angular diameter about two orders of magnitude smaller than the resolution achieved with lunar occultations. The fitted value of 4.514 ± 0.038 km s^{-1} for the perpendicular velocity in Fit #4 agrees within its error with that calculated from the ring geometry (4.505 km s^{-1}). We also note the high precision with which the parameters of interest can be obtained: the errors amount to just a few percent. However,

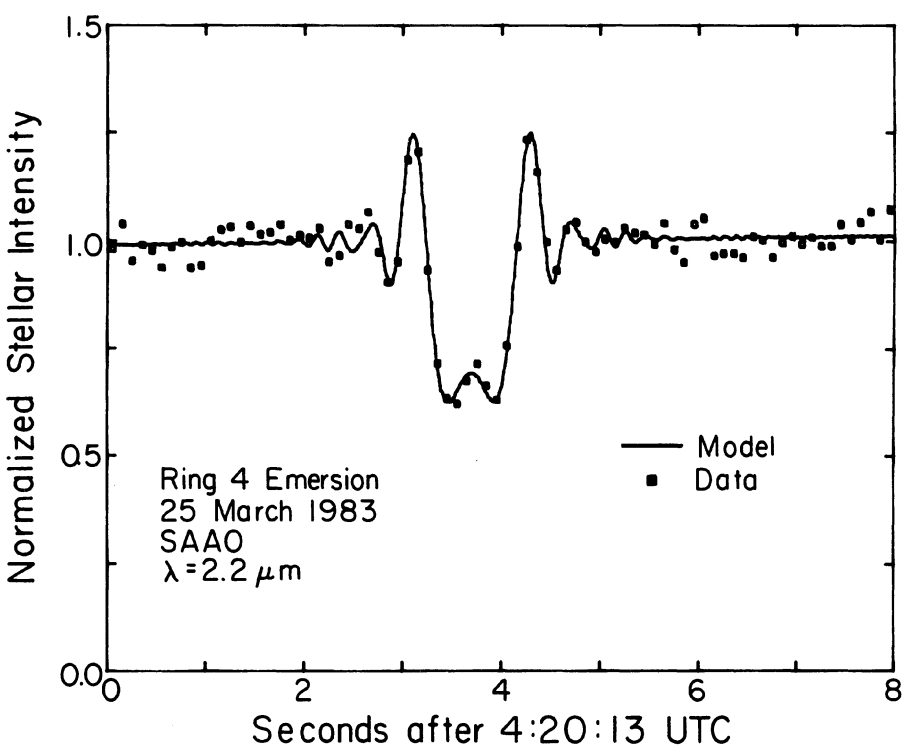

FIG. 3. Model fit to the emersion occultation profile of ring 4, observed on 23 March 1983 from the South African Astronomical Observatory (SAAO) (Elliot *et al.* 1984). The observations are well matched by the diffraction pattern of a sharp-edged translucent ring, convolved with the strip-brightness distribution of the occulted star.

TABLE II. Sample profile fits[a] (Ring 4–25 March 1983).

Fit Number	Parameter													
	$\bar{n}_f$ (s^{-1})	$\dot{n}_b$ (s^{-2})	$\bar{n}_*$ (s^{-1})	t_o (UTC)	T_o (s)	f_o	E (km)	A (km)	$v_\perp$ (km s^{-1})	T_* (s)	b	t_c(s)	rms error[b]
1	51363 ± 32	24 ± 13	(11194)	4:20:16.693 ± 0.005	0.234 ± 0.017	0.311 ± 0.031	[0.727]	[1.232]	(4.505)	(0.287)	(1.0)	(0.0)	0.0243
2	51363 ± 32	24 ± 13	(11194)	4:20:16.693 ± 0.005	0.234 ± 0.017	[0.311]	0.727 ± 0.031	[1.232]	(4.505)	(0.287)	(1.0)	(0.0)	0.0243
3	51363 ± 32	24 ± 13	(11194)	4:20:16.693 ± 0.005	0.234 ± 0.017	[0.311]	[0.727]	1.232 ± 0.055	(4.505)	(0.287)	(1.0)	(0.0)	0.0243
4	51361 ± 36	24 ± 13	9107 ± 3298	4:20:16.694 ± 0.005	0.265 ± 0.017	0.259 ± 0.195	[0.885]	[1.613]	4.514 ± 0.038	0.230 ± 0.037	(1.0)	(0.0)	0.0245
5	51317 ± 34	26 ± 14	4873 ± 235	4:20:16.694 ± 0.005	0.291 ± 0.018	(0.0)	[1.197]	---	4.519 ± 0.041	0.259 ± 0.035	(1.0)	(0.0)	0.0257

Notes

[a] Numbers in parentheses were held constant during the fit, and numbers in brackets were derived from other parameters in the fit.

[b] rms error per degree of freedom, in units of $\bar{n}_*$, for $\bar{n}_* = 11194\ s^{-1}$.

accurate photometric determination of the star level is critical. There is a very strong correlation between $\bar{n}_*$ and f_0, the fractional transmission (see Table IIIb). Systematic errors in $\bar{n}_*$ result in systematic errors in the determination of ring transmission. Finally, we note that the strong correlations among the parameters and the multidimensional nature of the parameter space being probed make least-squares fitting methods essential for accurate determination of ring widths and transmissions (and their uncertainties), especially for the narrowest rings.

IV. MULTIWAVELENGTH OBSERVATIONS

We have two multiwavelength data sets available for analysis. The first consists of optical observations of the occultation of SAO 158687 obtained at three wavelengths with the Kuiper Airborne Observatory (KAO) on 10 March 1977 (Elliot *et al.* 1977). Relevant parameters of the observations are given in Table IV and representative plots of the data and model fits are given in Fig. 4. In terms of signal-to-noise ratio, the data can be considered in two categories: the α, β, γ, δ, and ϵ rings have the greatest: the η, 4, 5, and 6 profiles are barely detectable.

The second data set was obtained at Cerro Tololo Interamerican Observatory (CTIO) on 22 April 1982, when the star KME 14 was occulted (Klemola *et al.* 1981). Observations at 0.88 μm were obtained with the 4-m telescope and observations at 2.2 μm were obtained with the 1.5-m telescope (Frogel and Elias 1980). The data were recorded (using the CTIO time series photometry program TSPHOT) on different computers, so that time synchronization was not precise, but appears to be good to about 0.05 s. Details of the observations are given in Table IV. For the infrared data, we made several recordings of the step response (of the electronics itself, not including the detector and chopper) so that the time constant could be fit separately, with the result: $t_c = 0.1535 \pm 0.0005$ s. Since these calibrations did not record the time that the step occurred, the fit for the time constant involved only the *shape* of the response of the system to a step input and was not constrained by the precise time of the step. The shapes of the model and calibration curves matched extremely well. However, any deviation of the actual system step response from our model could introduce a systematic error in the timing offset between our model midtimes and the actual midtimes.

Plots of some of the ring data and model fits are shown in Fig. 5. The IR data are considerably smoothed, due to the large time constant of the electronics. The deconvolved observations appear to be noisier than the 0.88-μm data, but this is an artifact of incomplete removal of the chopping frequency by the deconvolution process. Statistical tests reveal that the noise level relative to the signal from the star is very nearly the same for the 0.88-μm and 2.2-μm data.

We found no evidence for rings other than the nine already known, even though we probed the Uranian equatorial plane nearly to the orbit of Umbriel. Data recording with the infrared system ended at 05:53:10 UTC, when the starlight was passing at a distance of 243 000 km from Uranus in its equatorial plane. With the signal averaged to 1.0 s, no dips greater than about 2% of the unocculted star level were seen, other than at the (few) times of known guiding problems.

V. MODEL PROFILE FITS

We have applied the square-well model described in Secs. II and III to the KAO and CTIO observations in order to

TABLE III. Correlation matrices.

(a) Sample Profile Fits #1, 2, and 3

Parameter	$\bar{n}_f$	$\dot{n}_b$	t_o	T_o
$\bar{n}_f$	1.00	-0.14	0.00	0.25
$\dot{n}_b$	-0.14	1.00	0.16	-0.04
t_o	0.00	0.16	1.00	0.00
T_o	0.25	-0.04	0.00	1.00
f_o (Fit #1)	0.13	-0.02	0.00	0.86
E_o (Fit #2)	0.30	-0.05	0.00	0.84
A_o (Fit #3)	0.18	-0.03	0.00	0.02

(b) Sample Profile Fit #4

Parameter	$\bar{n}_f$	$\dot{n}_b$	$\bar{n}_*$	t_o	T_o	f_o	$v_\perp$	T_*
$\bar{n}_f$	1.00	-0.15	0.44	0.00	-0.05	0.44	0.02	-0.09
$\dot{n}_b$	-0.15	1.00	-0.06	0.02	0.01	-0.06	0.00	0.01
$\bar{n}_*$	0.44	-0.06	1.00	0.00	-0.45	0.99	0.04	-0.17
t_o	0.00	0.02	0.00	1.00	-0.01	0.00	0.00	0.02
T_o	-0.05	0.01	-0.45	-0.01	1.00	-0.33	-0.04	-0.39
f_o	0.44	-0.06	0.99	0.00	-0.33	1.00	0.04	-0.27
$v_\perp$	0.02	0.00	0.04	0.00	-0.04	0.04	1.00	0.02
T_*	-0.09	0.01	-0.17	0.02	-0.39	-0.27	0.02	1.00

compare the relative transmission of the rings at different wavelengths. The ring width and transmission are correlated parameters in the fits, and because we are primarily interested in estimating the *change* of transmission with wavelength, we fix the ring width at the same value for all fits to a given occultation profile, whatever the wavelength of the observation. Physically, this implies that the particle size distribution is uniform across the ring, an assumption that is consistent with the spirit of our square-well model. For each fit, the star level $\bar{n}_*$ is held fixed at the photometrically determined value, and the perpendicular velocity $v_\perp$ is fixed at the value determined from the ring geometry. The angular diameters of the occulted stars (see Table V) were estimated from Ridgway *et al.*'s (1980) occultation data, assuming fully limb-darkened stellar disks ($b = 1$).

For the KAO observations, we first fitted the sum of all three channels of data for each ring profile, allowing $\bar{n}_f$, $\dot{n}_b$, t_0, T_0, and A_0 to vary, and fixing values for $v_\perp$, T_*, b, and t_c [see Figs. 4(a) and 4(b)]. Because the projected stellar diameter is much larger than the Fresnel scale, diffraction effects are small, and we assumed that the weighting function $F(\lambda)$ was a delta function at $\lambda = 0.728$ μm for the summed data. We confirmed that the results do not change significantly when the detailed wavelength dependence of $F(\lambda)$ is taken into account. These fits to the summed data should give our best values for the mean width and midtime. The results are given in Table VI. Next, we fitted separately each of the three data channels for each profile, fixing the width and midtime at the values determined from the summed data, and allowing $\bar{n}_f$, $\dot{n}_b$, and A_0 to vary. The equivalent depths, A, and normal optical depths, τ_n, are given in Table VII.

We have analyzed the CTIO data similarly. We first obtained separated fits to the 0.88-μm and the deconvolved 2.2-μm profiles, and then averaged the widths and refitted the profiles with the width fixed at the mean value of the two individual fits [see Figs. 5(a) and 5(b)]. The results are given in Table VIII. Because of the small, but uncertain, timing offset between the two data sets, we have listed the midtimes for the 0.88-μm data only, which (unlike the 2.2-μm data) are not affected by a large instrumental time constant.

Except as indicated in the footnotes to Tables VI–VIII, the error bars are the formal errors of the fits, and do not account for uncertainties in parameters held fixed during the fits, such as the stellar diameter and the star level, $\bar{n}_*$.

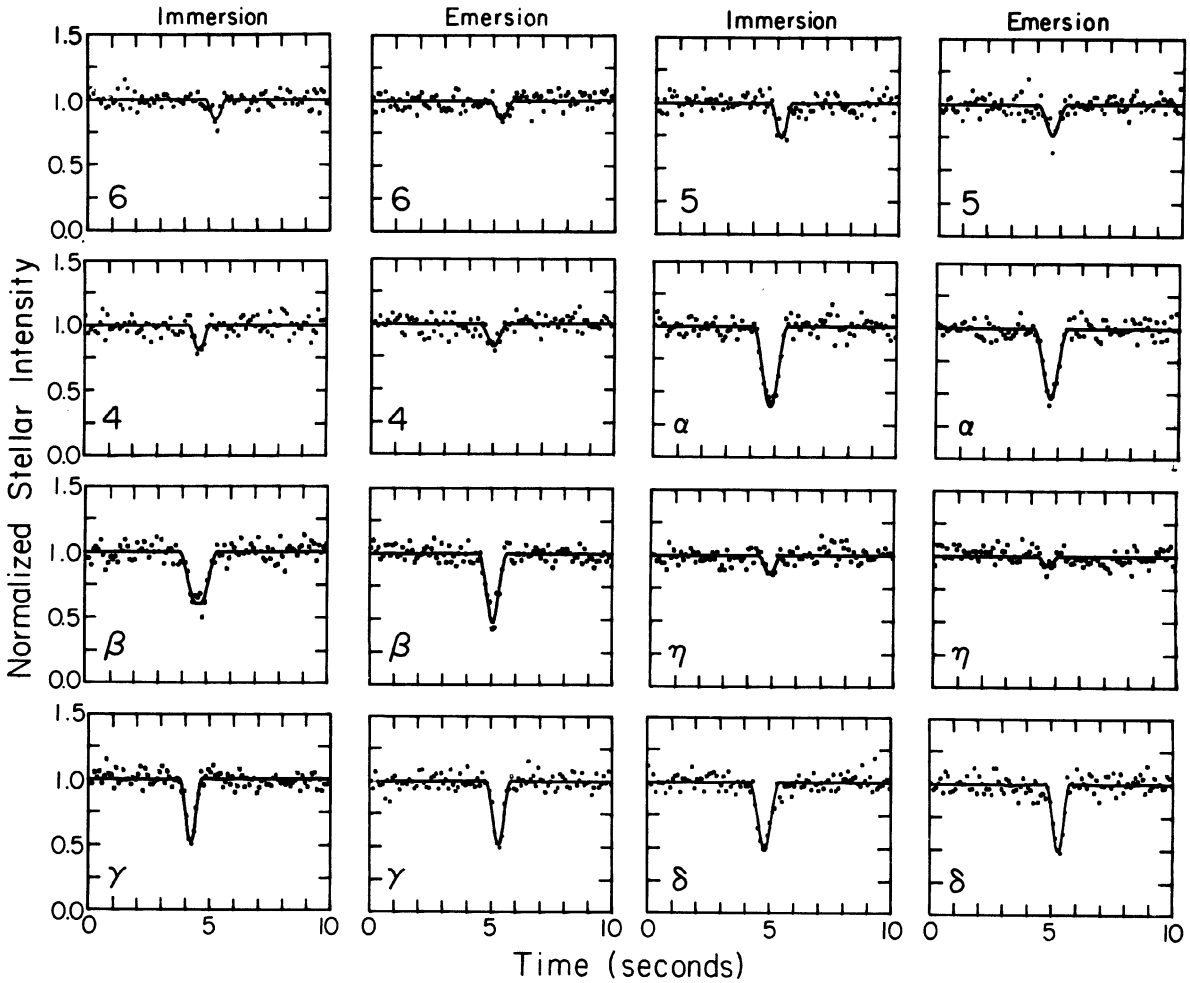

FIG. 4(a). Model fits to ring occultation profiles observed from the Kuiper Airborne Observatory (KAO) on 10 March 1977. Data from all three channels (see Table IV) have been summed, and are plotted at 0.1-s resolution.

VI. WAVELENGTH DEPENDENCE OF OPTICAL DEPTH

Using the results of the profile fits, we can investigate the wavelength dependence of the optical depth, and from these results we can establish the class of particle size distributions for the rings that would be consistent with our data. The most pronounced wavelength dependence of optical depth would be exhibited by particles with sizes comparable to the wavelengths of our observations—about 0.6–2.2 μm. We shall compare our data to two simple models: (i) a two-component model that has one population of micron-sized particles and another population of particles whose optical depth would be constant over the wavelength range of our observations, and (ii) a power law distribution of particle sizes, as used by Marouf *et al.* (1983) for Saturn's rings. Each of these comparisons will be in terms of the same quantity, the slope of the optical depth versus wave number, $d\tau/d(1/\lambda)$. For a polylayer ring, this derivative is related to the data through the equivalent depth by the equation

$$\frac{d\tau}{d(1/\lambda)} = \frac{1}{W}\frac{dA}{d(1/\lambda)}, \tag{14}$$

where W is the width of the ring and the slope $dA/d(1/\lambda)$ is determined by a linear least-squares fit to the values of A obtained from the profile fits.

In order to compare the optical depth of a ring as determined from occultation profiles probing different parts of the ring, we shall assume for the moment that a ring has constant linear mass density at all orbital longitudes, except for the negligible effects due to its small eccentricity. In this case, the equivalent depth A would not vary with location in the ring, and would vary only due to the wavelength dependence of the optical depth. We have plotted in Fig. 6 the equivalent depth A of the β and γ rings as a function of wavenumber $1/\lambda$, along with that of the best-fitting straight line. Since a slope less than zero violates the assumptions of the two-component model, which requires that A increase with $1/\lambda$ (under most circumstances), a negative slope must be interpreted as placing an upper limit on the wavelength dependence of optical depth. A serious flaw in this analysis is that the equivalent depth of several rings is demonstrably not independent of orbital longitude. For example, even though they are at comparable wavelengths, the equivalent depths of

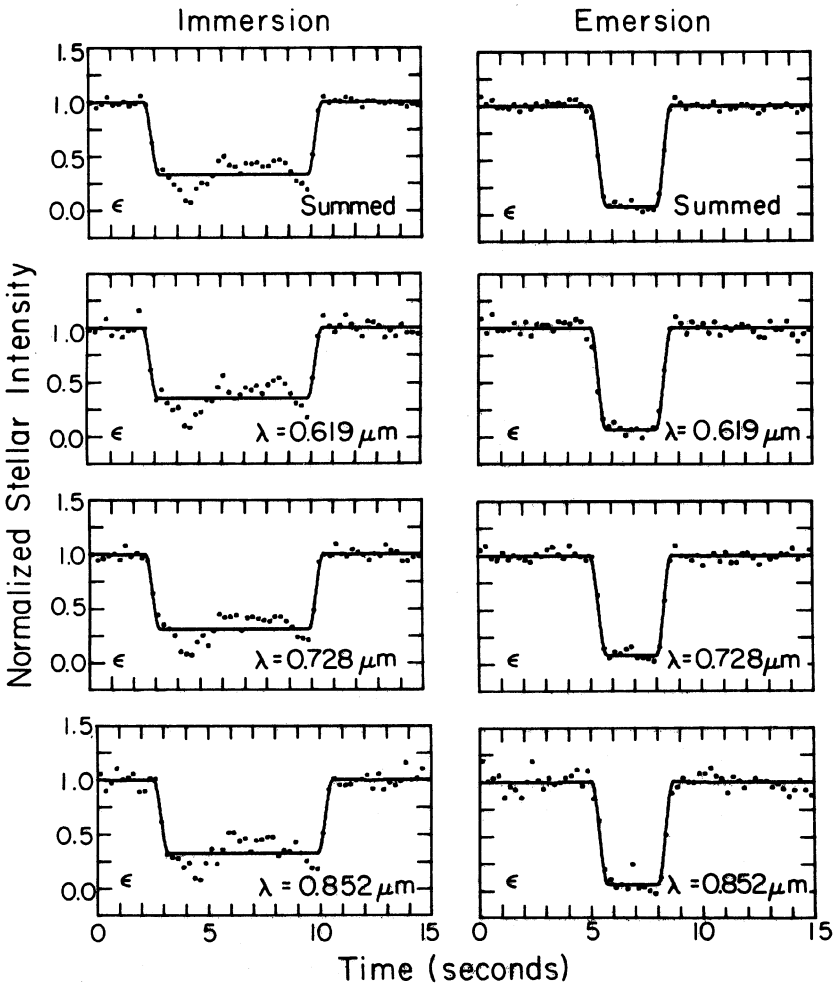

FIG. 4(b). Model fits to ϵ ring profiles observed from the Kuiper Airborne Observatory (KAO) on 10 March 1977. The top figures show the summed data from all three channels (see Table IV). The data for each channel are shown separately in the lower figures, along with the best model fit. All observations are plotted at 0.1-s resolution.

TABLE IV. Observations.

Observatory	Telescope Aperture (meters)	Focal Plane Aperture (arcsec)	Center Wavelength (μm)	Passband (FWHM, μm)	Mag Tape Recording Interval (Sec)	Date	Observation Interval (UTC)
KAO	0.9 m	46	0.619 0.728 0.852	0.008 0.020 0.021	0.01	10 March 1977	$20^h\ 05^m\ 40^s$ - $22^h\ 17^m\ 40^s$
CTIO	1.5 m	20	2.2	0.40	0.01*	22 April 1982	$01^h\ 03^m\ 27^s$ - $05^h\ 53^m\ 10^s$
	4.0 m	37.5	0.88	0.036	0.01	22 April 1982	$00^h\ 56^m\ 24^s$ - $04^h\ 00^m\ 10^s$

* The signal was chopped at 10 Hz with a focal plane chopper and the data recording electronics had a measured time constant of 0.1535 ± 0.0005 seconds.

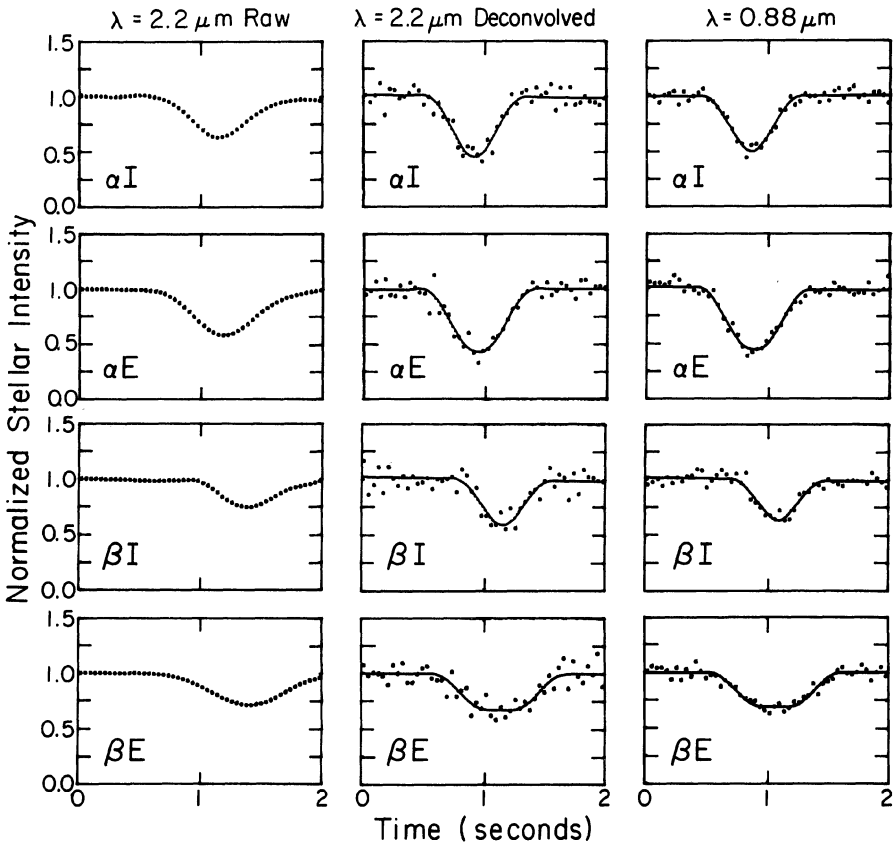

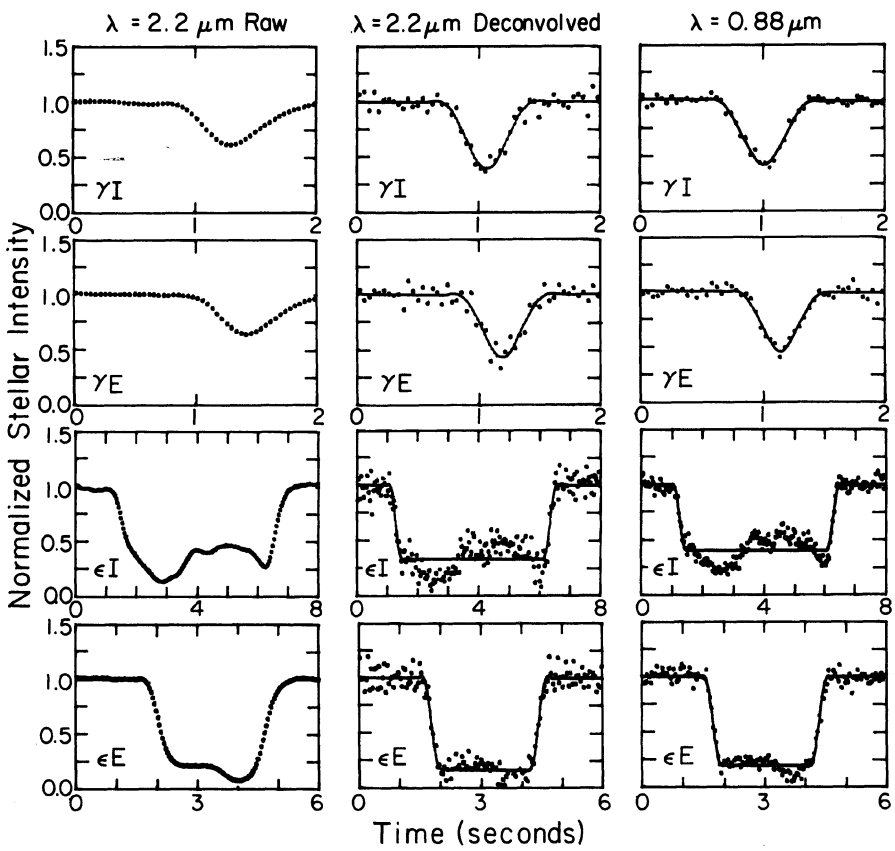

FIG. 5. Model fits to ring occultation profiles obtained at CTIO on 22 April 1982. *I* and *E* stand for immersion and emersion, respectively. The 2.2-μm data are plotted on the left-hand side. Note the smoothing effect of the time constant of the observing electronics. In the middle column of figures, the impulse response function has been deconvolved from the raw 2.2-μm data, and the best-fitting model profile is shown. At right, the 0.88-μm observations are plotted with the best-fitting model.

TABLE V. Adopted stellar diameters.

Occultation Date	Occulted Star	Angular Diameter (milliarcsec)	Projected Diameter at Uranus (km)
10 March 1977	SAO 158687	0.55	7.151
22 April 1982	KME 14	0.54	7.056

TABLE VI. Fit results for summed KAO profiles.[a]

Ring Profile	Midtime (t_o, UTC on 10 March 1977)	Duration (T_o, sec)	Width (W, km)	Equivalent Depth (A, km)	Fractional Transmission (f_o)	True Anomaly[b] (θ, deg)
6I	20:24:48.290 ± 0.007	0.123 ± 0.023	1.42 ± 0.27	1.04 ± 0.32	[0.44]	157.9
6E	21:41:48.334 ± 0.023	0.233 ± 0.057	2.68 ± 0.66	0.80 ± 0.21	[0.70]	265.4
5I	20:24:13.155 ± 0.012	0.230 ± 0.015	2.67 ± 0.18	1.86 ± 0.32	[0.46]	231.0
5E	21:42:18.653 ± 0.017	0.458 ± 0.038	5.30 ± 0.44	1.52 ± 0.22	[0.71]	339.2
4I	20:23:51.744 ± 0.012	0.193 ± 0.035	2.25 ± 0.41	1.24 ± 0.28	[0.54]	275.5
4E	21:42:47.010 ± 0.031	0.432 ± 0.075	5.02 ± 0.87	1.05 ± 0.20	[0.78]	24.3
αI	20:20:53.828 ± 0.007	0.705 ± 0.013	8.43 ± 0.16	7.10 ± 0.46	[0.38]	69.5
αE	21:45:51.705 ± 0.008	0.665 ± 0.018	7.92 ± 0.22	5.22 ± 0.38	[0.45]	182.2
βI	20:19:33.687 ± 0.013	0.890 ± 0.028	10.72 ± 0.34	4.75 ± 0.35	[0.60]	174.2
βE	21:47:06.074 ± 0.009	0.474 ± 0.023	5.70 ± 0.27	4.54 ± 0.42	[0.38]	288.5
ηI	20:17:32.929 ± 0.019	0.294 ± 0.051	3.59 ± 0.62	0.82 ± 0.20	[0.77]	267.9
ηE	21:49:08.713 ± 0.016	0.098 ± 0.041	1.19 ± 0.51	0.40 ± 0.20	[0.66]	24.6
γI	20:16:57.230 ± 0.004	0.262 ± 0.011	3.21 ± 0.14	5.24 ± 0.97	[0.15]	312.6
γE	21:49:44.309 ± 0.006	0.316 ± 0.011	3.86 ± 0.14	4.55 ± 0.61	[0.24]	69.9
δI	20:16:02.830 ± 0.010	0.559 ± 0.023	6.88 ± 0.29	4.73 ± 0.38	[0.46]	261.1
δE	21:50:38.269 ± 0.007	0.263 ± 0.016	3.23 ± 0.20	7.36 ± 2.53	[0.06]	19.4
εI	20:11:46.544 ± 0.007	7.373 ± 0.014	92.60 ± 0.18	88.86 ± 2.35	[0.33]	179.1
εE	21:54:05.869 ± 0.004	2.937 ± 0.008	36.70 ± 0.09	79.07 ± 4.98	[0.07]	301.2

[a] Numbers in brackets were derived from other parameters in the fit.

[b] Determined from the ring orbit model of French et al. (1982).

TABLE VII. Optical depths from KAO observations.

Ring Profile	Channel 1 (0.619 μm)		Channel 2 (0.728 μm)		Channel 3 (0.852 μm)	
	Equivalent Depth (A, km)	Normal Optical Depth (τ_n)	Equivalent Depth (A, km)	Normal Optical Depth (τ_n)	Equivalent Depth (A, km)	Normal Optical Depth (τ_n)
6I	0.91 ± 0.49	0.64 ± 0.34	1.19 ± 0.43	0.84 ± 0.30	1.08 ± 0.60	0.76 ± 0.42
6E	0.85 ± 0.37	0.32 ± 0.14	0.64 ± 0.23	0.24 ± 0.09	1.26 ± 0.46	0.47 ± 0.17
5I	1.83 ± 0.55	0.69 ± 0.21	2.30 ± 0.47	0.86 ± 0.18	1.06 ± 0.41	0.40 ± 0.15
5E	1.25 ± 0.36	0.24 ± 0.07	1.72 ± 0.29	0.32 ± 0.05	1.80 ± 0.42	0.34 ± 0.08
4I	0.96 ± 0.42	0.43 ± 0.19	1.42 ± 0.36	0.63 ± 0.16	2.17 ± 0.80	0.96 ± 0.35
4E	0.83 ± 0.33	0.17 ± 0.07	1.26 ± 0.26	0.25 ± 0.05	1.13 ± 0.39	0.23 ± 0.08
αI	7.54 ± 0.90	0.89 ± 0.11	6.55 ± 0.56	0.78 ± 0.07	6.26 ± 0.78	0.74 ± 0.09
αE	4.79 ± 0.65	0.61 ± 0.08	5.66 ± 0.51	0.71 ± 0.06	5.59 ± 0.77	0.71 ± 0.10
βI	4.66 ± 0.61	0.43 ± 0.06	4.65 ± 0.43	0.43 ± 0.04	4.78 ± 0.64	0.45 ± 0.06
βE	4.62 ± 0.73	0.81 ± 0.13	4.32 ± 0.49	0.76 ± 0.09	5.08 ± 0.91	0.89 ± 0.16
ηI	0.82 ± 0.36	0.23 ± 0.10	0.90 ± 0.27	0.25 ± 0.07	0.63 ± 0.34	0.17 ± 0.10
ηE	1.16 ± 0.73	0.98 ± 0.61	0.36 ± 0.26	0.30 ± 0.22	0.27 ± 0.33	0.23 ± 0.28
γI	4.54 ± 1.27	1.42 ± 0.40	4.73 ± 1.01	1.47 ± 0.31	6.56 ± 2.68	2.04 ± 0.84
γE	5.12 ± 1.27	1.33 ± 0.33	4.32 ± 0.73	1.12 ± 0.19	3.65 ± 0.84	0.95 ± 0.22
δI	4.53 ± 0.35	0.66 ± 0.09	5.10 ± 0.51	0.74 ± 0.07	4.33 ± 0.68	0.63 ± 0.10
δE	8.80 ± 6.26	2.73 ± 1.94	6.19 ± 1.72	1.92 ± 0.53	6.51 ± 2.89	2.02 ± 0.89
εI	83.09 ± 3.73	0.90 ± 0.04	93.56 ± 3.09	1.00 ± 0.03	90.13 ± 4.10	0.96 ± 0.04
εE	81.14 ± 9.33	2.21 ± 0.25	76.28 ± 5.57	2.08 ± 0.15	86.25 ± 11.15	2.35 ± 0.30

rings α, β, and δ are quite different for the summed KAO profiles and the 0.88-μm CTIO profiles (see Tables VI and VIII). The differences in A between immersion and emersion profiles obtained at the same observatory are much greater than their error bars for these rings, so that the variations can not be dismissed simply as the result of systematic calibration errors in one set of observations. This makes it difficult to draw firm conclusions from the comparison of different profiles of a given ring. To proceed further, we will henceforth restrict our attention to the CTIO observations, which span a significant range in wavelength and have a higher signal-to-noise ratio than the KAO data. Furthermore, we shall examine the wavelength dependence of τ_n for the immersion and emersion profiles separately.

To obtain a crude idea of the possible populations of particles, we shall adopt a simplified two-component model. One population consists of particles so large that their combined optical depth has the constant value $\tau_{\rm large}$ over the wavelengths spanned by our observations. The second population consists of particles small enough so that their optical depth, $\tau_{\rm small} \propto (1/\lambda)$. The largest particle radius for which this proportionality is valid depends on the complex index of refraction of the particles. Within a factor of a few, we can set this maximum radius as 0.5 μm for the Cerro Tololo observations; for most physically plausible particles, the maximum radius is $\lesssim 0.2$ μm.

The ratio $r_\tau(\lambda)$ of the optical depth contributed by the small particles to that contributed by the large particles is given by the equation

$$r_\tau(\lambda) = \frac{\tau_{\rm small}(\lambda)}{\tau_{\rm large}}. \tag{15}$$

For the observations at two wavelengths, the above equation can be written in terms of the wavelengths and fitted equivalent depths:

$$r_\tau(\lambda_1) = \frac{[A(\lambda_1) - A(\lambda_2)]}{\left[A(\lambda_2) - \left(\frac{\lambda_1}{\lambda_2}\right) A(\lambda_1)\right]}, \tag{16}$$

where λ_1 (0.88 μm) and λ_2 (2.2 μm) are the wavelengths of the two profiles used to determine the equivalent depths. Values of r_τ(0.88 μm) for the two-component model for the CTIO profiles are given in Table IX. In terms of the two-component model, we conclude that (for the ring system as a whole) an upper limit of 0.10 can be placed on the relative contribution of small ($a < 0.5$ μm) and large ($a \gg 0.5$ μm) particles to the optical depth at 0.88 μm. Since small particles have higher optical depth per unit mass than large particles, this implies that over 90% of the ring mass is in particles of approximately micron size or larger.

TABLE VIII. Fit results for CTIO profiles.[a]

Ring Profile	Midtime[b] (T_0, UTC on 22 April 1982)	Duration[c] (T_0, sec)	Width[c] (W, km)	Equivalent Depth (A, km)[d] λ = 0.88 μm	λ = 2.2 μm	Fractional Transmission (f_0)[d] λ = 0.88 μm	λ = 2.2 μm	Normal Optical Depth λ = 0.88 μm	λ = 2.2 μm	True Anomaly[e] (θ, deg)
6I	1:42:41.517 ± 0.028[f]	(0.17)	---	---	---	(0.5)	---	---	---	24.1
6E	2:51:54.397 ± 0.009	(0.17)	---	---	---	(0.5)	---	---	---	157.9
5I	1:42:15.747 ± 0.009	(0.27)	---	---	---	(0.5)	---	---	---	266.4
5E	2:52:10.962 ± 0.014	0.236 ± 0.057	4.04 ± 0.97	1.31 ± 0.13	1.21 ± 0.13	[0.71]	[0.74]	[0.32]	[0.30]	40.5
4I	1:41:56.511 ± 0.015	0.188 ± 0.028	3.20 ± 0.49	1.13 ± 0.14	1.21 ± 0.14	[0.70]	[0.68]	[0.35]	[0.38]	87.5
4E	2:52:36.407 ± 0.015	0.285 ± 0.037	4.90 ± 0.64	1.26 ± 0.13	1.29 ± 0.13	[0.77]	[0.76]	[0.26]	[0.26]	222.2
αI	1:39:51.863 ± 0.007	0.377 ± 0.016	6.48 ± 0.28	4.62 ± 0.23	5.40 ± 0.23	[0.48]	[0.43]	[0.71]	[0.83]	294.3
αE	2:54:37.878 ± 0.007	0.471 ± 0.014	8.16 ± 0.24	6.40 ± 0.30	6.56 ± 0.30	[0.44]	[0.43]	[0.78]	[0.80]	71.1
βI	1:38:57.584 ± 0.011	0.350 ± 0.029	6.04 ± 0.49	2.85 ± 0.21	3.39 ± 0.21	[0.62]	[0.57]	[0.47]	[0.56]	328.1
βE	2:55:33.067 ± 0.013	0.654 ± 0.023	11.37 ± 0.39	4.05 ± 0.23	4.31 ± 0.23	[0.69]	[0.68]	[0.36]	[0.38]	105.9
ηI	1:37:29.005 ± 0.026	(0.17)	---	---	---	(0.81)	---	---	---	113.2
ηE	2:56:59.683 ± 0.021	(0.17)	---	---	---	(0.75)	---	---	---	252.2
γI	1:37:03.011 ± 0.005	0.360 ± 0.013	6.24 ± 0.22	5.76 ± 0.26	6.09 ± 0.26	[0.39]	[0.37]	[0.92]	[0.98]	269.4
γE	2:57:25.143 ± 0.006	0.308 ± 0.020	5.39 ± 0.34	4.70 ± 0.28	5.36 ± 0.28	[0.40]	[0.36]	[0.89]	[0.99]	49.0
δI	1:36:24.393 ± 0.010	0.282 ± 0.031	4.90 ± 0.54	2.41 ± 0.18	2.29 ± 0.18	[0.61]	[0.62]	[0.49]	[0.47]	15.3
δE	2:58:04.128 ± 0.008	0.419 ± 0.017	7.35 ± 0.30	4.63 ± 0.24	4.38 ± 0.24	[0.52]	[0.54]	[0.63]	[0.60]	155.5
εI[g]	1:33:22.755 ± 0.007	5.051 ± 0.009	88.42 ± 0.15	79.54 ± 1.87	96.58 ± 1.87	[0.40]	[0.33]	[0.90]	[1.09]	141.8
εE[g]	3:00:40.038 ± 0.004	2.615 ± 0.007	46.14 ± 0.13	72.58 ± 1.72	82.08 ± 1.72	[0.20]	[0.16]	[1.57]	[1.78]	284.4

a Unless otherwise noted all errors are formal errors from the least squares fits; all quantities in parenthesis were held fixed during the fit; numbers in brackets were derived from other parameters in the fit.
b Determined from fit to λ = 0.88 μm observations, except as noted.
c Average of results of separate fits to λ = 0.88 μm and λ = 2.2 μm observations with $\bar{n}_b$, $\dot{n}_b$ t_0, T_0, and A_0 as free parameters. Errors in T_0 and W are $1/\sqrt{2}$ times the formal errors in the fits to the λ = 0.88 μm data alone.
d Determined from separate fits to λ = 0.88 μm and λ = 2.2 μm data with $\bar{n}_b$, $\dot{n}_b$, and A_0 as free parameters, t_0 fixed at final values from fits described in note c, above, and T_0 fixed at the value given in the table. Errors in A for λ = 2.2 μm fits are set to values for λ = 0.88 μm fits. See text for details.
e Determined from ring orbit model of French et al. (1982).
f Determined from fit to λ = 2.2 μm data, and corrected for timing offset between λ = 2.2 μm and λ = 0.88 μm observations.
g $\dot{n}_b$ fixed at zero.

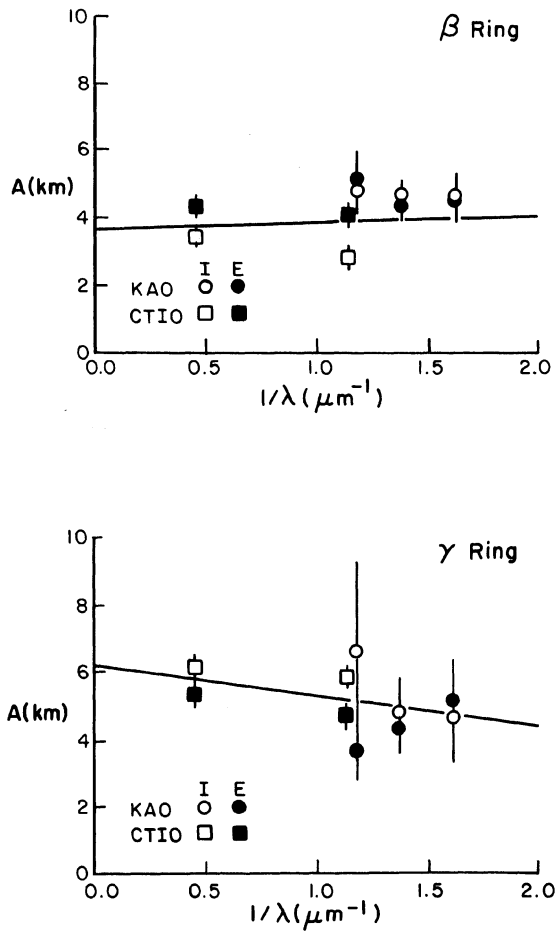

FIG. 6. Wavelength dependence of ring opacity. The equivalent depth A is plotted as a function of wavenumber $1/\lambda$ for the β and γ rings. The best-fitting two-component opacity model for each ring is shown as a straight line. See the text for details.

A simple physical model, used widely in the study of Saturn's rings (see Marouf *et al.* 1983, and references cited therein), is a power law distribution of particle sizes of the form

$$n(a) = n(a_0)\left[\frac{a}{a_0}\right]^{-q}, \tag{17}$$

where $n(a)da$ is the column density of particles with radii between a and $a + da$, a_0 is an arbitrary reference radius, and q is the power law index; the distribution applies between two cutoff sizes, $a_{\max}$ and $a_{\min}$. In general, the wavelength dependence of the optical depth corresponding to a polylayer of such particles is related to the extinction efficiency of the particles, which in turn depends upon their shape and refractive index and can be computed from Mie scattering theory. Based on such calculations, Marouf *et al.* (1983) strongly constrained the power law index, q, appropriate for Saturn's rings for particles in the centimeter- to meter-size range. We do not have enough information about Uranian ring properties to warrant such detailed calculations here.

The extinction cross section of small particles is roughly proportional to their volume, while for large particles it is roughly twice their geometrical cross section, if the diffracted component is not included in the field of view of the detector (see van de Hulst 1957). The constraints of Table IX can be satisfied by plausible values of $a_{\max}$ and $a_{\min}$ for power law distributions with index $q \lesssim 3$.

VII. DISCUSSION

Our constraints on allowed particle sizes can be compared with those from the phase function and spectra of the rings. This comparison is essentially limited to the ϵ ring, since the photometric data, obtained with a spatial resolution several thousand times coarser than the occultation data, refer to the light reflected by all the rings together, and the ϵ ring contains most of the effective area. Pang and Nicholson (1984) have concluded that the observed spectrum of the rings, spanning the wavelength range 0.7–3.9 μm, most closely matches that of carbon black–except for a discrepancy at 3.9 μm. From the flatness of the spectrum, they conclude that the reflectance is not dominated by particles smaller than 0.1 μm in size. This limit is close to that set by the occultation profiles; in fact, the underlying physical argument is basically the same in both cases. Pang and Nicholson (1984) use the flat phase curve observational uncertainty to infer that the reflectance of the rings contains only a small contribution from particles larger than 10 μm (assuming they are not spherical). Hence they conclude that most Uranian ring particles are composed of carbon black between 0.1 and 10 μm in size.

Both the occultation profiles and the flat albedo of the rings indicate that only a very small fraction of the mass of the rings can be in submicron particles. An upper limit on the particle size is provided only by the lack of a pronounced opposition effect. Stronger limits could be provided by more accurate searches for an opposition effect or occultations at longer wavelengths. The upper size limit implies that most of the ring area is comprised of micron-sized particles, but even with this constraint it is possible for much of the mass to be in larger particles. In fact, the opacities for the α, β, and ϵ rings obtained by Elliot and Nicholson (1984), assuming that the uniform precession of these rings is due to self-gravity, would imply that "typical" particles have radii of a few centimeters.

Another factor to consider when constructing possible particle distributions for the Uranian rings is the magnitude of the confining torque needed, presumably from shepherd satellites, to maintain the ring against the eroding torque from the Poynting-Robertson effect. One can not require larger confining torques from the shepherd satellites than would be consistent with present observed limits on the perturbations of the ring orbits (Freedman *et al.* 1983).

We can compare our knowledge of the largest Uranian ringlet, the ϵ ring, with Saturn's eccentric ringlet in the Maxwell gap at 1.45 R_s. As pointed out by Esposito *et al.* (1983), this ringlet closely resembles the ϵ ring in its maximum and minimum widths (26 and 100 km), its inferred mass (5×10^{18} gm), and its range of optical depths in visible light (1.5–2.0). However, its albedo is much greater than that of the ϵ ring, and its optical depth is peaked near the middle of the ring, rather than at its edges. From a combined analysis of occultation data at radio and visible wavelengths, Esposito *et al.* (1983) conclude that at least one-half of the ring cross section is due to particles smaller than 1 cm. However, the substantial optical depth at the 13-cm radio wavelength implies that a large fraction of the particles have sizes greater than 1 cm, which would be fundamentally different from the 0.1–10

TABLE IX. Wavelength dependence of optical depth from CTIO observations.

Ring Profile	r_τ(0.88 μm)	$\sigma_{0.00}(r_\tau)^a$	$\sigma_{0.05}(r_\tau)^b$
5E	0.15	0.07	0.08
4I	-0.10	0.04	0.05
4E	-0.03	0.01	0.01
αI	-0.22	0.04	0.06
αE	-0.04	0.01	0.02
βI	-0.24	0.05	0.07
βE	-0.10	0.02	0.03
γI	-0.09	0.01	0.03
γE	-0.19	0.04	0.06
δI	0.10	0.03	0.04
δE	0.10	0.02	0.04
εI	-0.26	0.02	0.06
εE	-0.17	0.01	0.07

[a] For $\sigma(n_*)/n_* = 0.00$

[b] For the more realistic assumption that $\sigma(n_*)/n_* = 0.005$

μm sizes discussed by Pang and Nicholson (1984) for the Uranian rings.

VIII. CONCLUSIONS

While the square-well model does not perfectly describe all the ring-occultation profiles, it does surprisingly well for most. Until better models become available, we can use least-squares fitting of the square-well model to obtain highly precise midtimes, widths, and fractional transmissions of the rings. We achieve precisions of tens of meters in the placement of a ring segment, one-hundred meters in the width of a segment, and a few hundredths in its fractional transmission. These results promise nearly an order of magnitude improvement in our ability to compare the ring structure and kinematics with dynamical models.

For example, we note that the midtimes obtained from our model fits for the KAO (Table VI) differ in some cases by nearly 0.1 s from the times derived with other methods by Elliot *et al.* (1978). The times from the model fits here should be the more reliable; this suggests that the discrepancy between the formal errors in the midtimes from the model profile fits (0.01 s) and the rms residual (0.14 s) from our latest ring-orbit model (French *et al.* 1982) could be due, at least in part, to errors in our previous determinations of the midtimes.

Another line of investigation opened up by the results of the model fits is determining why the fitted equivalent depths for different segments of the same ring disagree by several times their formal errors. These disparities indicate an apparent longitudinal clumping of ring material, which could be due to longitudinal waves excited by shepherd satellites, the presence of kilometer-sized ring particles, or the concentration of ring material into high optical depth "subringlets" that have variable radial spacing around the ring. These latter two possibilities would become apparent only with higher spatial resolution.

A third area of interest that can be pursued with the results of the model fits concerns potential apsidal twists and inclination gradients in the ring orbits. The errors in the fitted widths seem small enough to allow a search for these features with great enough precision to be interesting; these subjects will be the topic of Paper II.

To realize the full potential of information contained in the ring profiles from future occultations, observers should record their data unchopped. This greatly simplifies the model fitting and allows a straightforward interpretation of the errors in the model fits. Continuous observation of the source also improves the signal-to-noise ratio by a factor ranging between 2 and $\sqrt{2}$, depending on whether the main source of noise is random noise from the background or the source itself. Direct measurement of the signal level from the star alone, immediately following each ring occultation, as was done by Elliot *et al.*(1984), allows this quantity to be fixed during the model fit; fixing the star level greatly reduces the errors in fitted widths and fractional transmissions (see Table II).

Within the precision of our data, we find no evidence for variation of the optical depths of the Uranian rings over the wavelength range 0.88–2.2 μm. This result would be consistent with an inverse power law distribution of particle radii with index $\lesssim 3$. Another interpretation is that less than 10% of the optical depth in this spectral region is contributed by particles less than 0.5 μm in radius. Our results may not be consistent, however, with Pang and Nicholson's (1984) conclusion that most of the ring particles lie within the 0.1–10 μm size range, which was based on the spectrum and the lack of opposition effect exhibited by the rings. The next steps in the investigation of the particle size distribution of Uranian rings would be to determine what particle distributions, if any, would be consistent with all present information—spectra, the phase function, and the occultation data. More accurate measurements of the photometric phase function would also be in order since this is the evidence that has been used to infer a small population of particles larger than 10 μm.

We thank Arturo Gomez, Ricardo Gonzalez, Gabriel Martin, Daniel Maturana, Mauricio Navarrete, and Oscar Saa for assistance with setting up our equipment and making the observations at Cerro Tololo. Brooke Gregory helped with the equipment and observations on the 1.5-m telescope. Doug Mink and Ted Dunham provided helpful discussions; Karen Lasky assisted with the data analysis. As referee, Phil Nicholson made several helpful comments. This work was supported in part by NASA Grants Nos. NSG 2342, NSG 7526, NGL 05-002-140, and by NSF Grant No. AST 8209825.

APPENDIX: DIFFRACTION BY A PARTIALLY OPAQUE RING

We consider a flat ring composed of opaque particles that are uniformly distributed over its width W. If the particles are small compared to the Fresnel scale ($\sqrt{\lambda D}$) for an incident plane wave, where λ is the wavelength of the light and D is the distance from the ring to the observer, then the ring can be considered as a gray screen of average transmission f_0, where f_0 is the fraction of the area not covered by particles as would be seen by the observer. The apparent velocity of the occulted star perpendicular to the ring segment is $v_\perp$. The duration of the ring occultation is T_0, and the midtime of the

occultation by the ring is t_0. We define the following dimensionless variables:

$$z = \frac{\sqrt{2} v_\perp (t - t_0)}{\sqrt{D\lambda}}, \tag{A1}$$

$$\Delta z = \frac{v_\perp T_0}{\sqrt{2D\lambda}}, \tag{A2}$$

$$p = 1 - \sqrt{f_0}. \tag{A3}$$

The intensity of the observed occultation profile is found by multiplying the amplitude of the transmitted plane wave by the factor $\sqrt{f_0}$ and carrying out the Fresnel diffraction calculation (Born and Wolf 1964). In terms of the Fresnel integrals $C(z)$ and $S(z)$ (Rossi 1959; Abramowitz and Stegun 1965), we can write the following equation for $P(t, t_0, f_0, T_0, v_\perp, D, \lambda)$, the occultation profile for the ring normalized to 1.0 for a perfectly transmitting ring:

$$P(t, t_0, f_0, T_0, v_\perp, D, \lambda) = \frac{1}{2}\{[1 + p\,[C(z - \Delta z) - C(z + \Delta z)]]^2 + [1 + p\,[S(z - \Delta z) - S(z + \Delta z)]]^2\}. \tag{A4}$$

Calculation of the Fresnel functions is carried out by defining $C(z)$ and $S(z)$ in terms of the auxiliary functions $f(z)$ and $g(z)$ (Abramowitz and Stegun 1965):

$$C(z) = \frac{1}{2} + f(z)\sin\left(\frac{\pi}{2}z^2\right) - g(z)\cos\left(\frac{\pi}{2}z^2\right), \tag{A5}$$

$$S(z) = \frac{1}{2} - f(z)\cos\left(\frac{\pi}{2}z^2\right) - g(z)\sin\left(\frac{\pi}{2}z^2\right). \tag{A6}$$

We use the polynomial approximations to $f(z)$ and $g(z)$ for $0 \leqslant z \leqslant \infty$ given by Peterson (1979):

$$f(z) = \frac{1 + 0.92542z + 0.31166z^2}{2 + 1.91425z + 3.10846z^2 + 0.979113z^3}, \tag{A7}$$

$$g(z) = \frac{1 + 1.00622z}{2 + 5.96427z + 9.66481z^2 + 5.01981z^3 + 9.93095z^4}. \tag{A8}$$

For values of $z < 0$, we use the relations $C(-z) = -C(z)$ and $S(-z) = -S(z)$.

For $0 \leqslant z \leqslant 5$, a comparison of values obtained for the Fresnel functions calculated with these approximations and the tables given by Abramowitz and Stegun (1965) revealed a maximum error of 4×10^{-4}. Calculation of a typical profile showed agreement to better than 0.1% with calculations by the numerical code described by French and Lovelace (1983). Another method for computing the Fresnel integrals that we have found to be more accurate, but have not yet implemented with efficient code, is described by Lotsch and Gray (1964).

The diffraction patterns of partially opaque rings exhibit several properties that we illustrate in Fig. 7. In the limit of an infinitely narrow opaque ring [Fig. 7(a)], the main lobe of the profile reaches a lower limit to the full width at half maximum of approximately 1.5 $\sqrt{\lambda D}$, and the amount of light removed from the main lobe is twice the geometric cross section of the ring (see van de Hulst 1957). For a proper choice of width [Figs. 7(b) and 7(c)], the transmitted light from both sides of the ring can constructively interfere, producing beats and fringes of much greater amplitude than are possible with diffraction from a single edge (such as the lunar limb). For a ring that is broad in comparison with the Fresnel scale [Fig. 7(d)], the diffraction pattern on each side closely resembles that from a single edge. By comparing Figs. 7(a) and 7(e), we see that the diffraction pattern from a non-opaque ring has substantially reduced fringe amplitudes and less steep edges; it also exhibits "negative" fringes on the lower transmitting side of each edge.

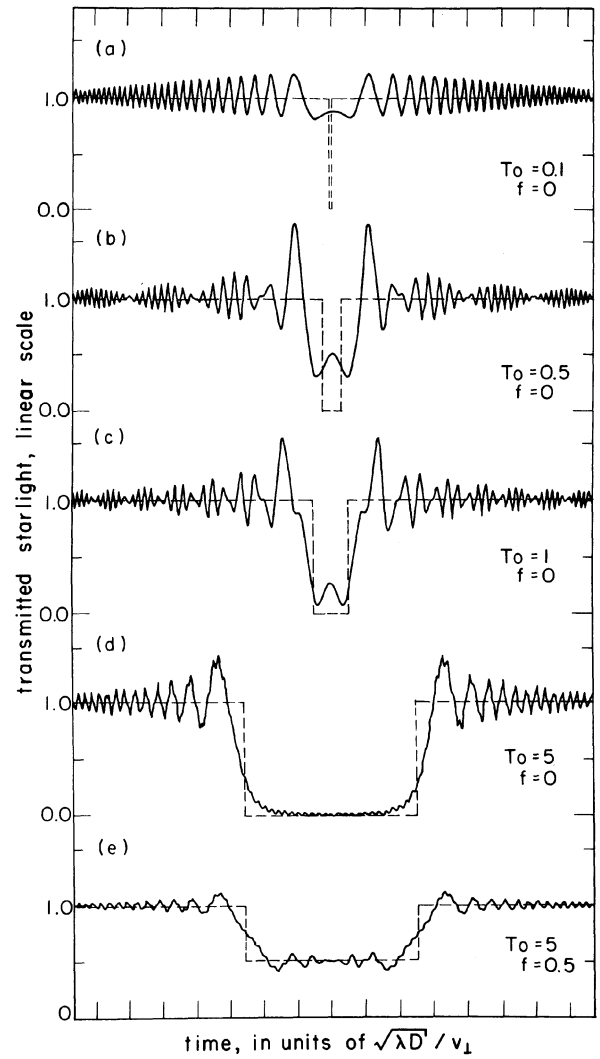

FIG. 7. Model occultation profiles. For each section of the figure, the dashed line shows the starlight transmitted through a ring, neglecting diffraction effects, as a function of time (given in units of the Fresnel scale divided by the velocity perpendicular to the edge of the ring). The solid line shows the transmitted starlight versus time with diffraction effects included. The quantity T_0 is the width of the ring in the indicated units, and f is the fractional transmission of the ring. Panel (a) shows the limiting width of the diffracted profile for a narrow ring, and panels (b) and (c) show broader rings, with beats and large amplitudes of the fringes caused by interference of the light wave coming from both sides of the ring. For an even broader ring, compared with the Fresnel scale, the diffraction pattern on each side resembles that of a single edge, such as the limb of the moon. If the ring is not totally opaque, as shown in panel (e), the amplitudes of the fringes are less, the edges of the profile are not as sharp, and "negative" diffraction fringes appear.

REFERENCES

Abramowitz, M., and Stegun, I. A. (1965). *Handbook of Mathematical Functions* (Dover, New York).

Born, M., and Wolf, E. (1964). *Principles of Optics*, 2nd ed. (MacMillan, New York), p. 428.

Clifford, A. A. (1973). *Multivariate Error Analysis* (Applied Science Publishers, London).

Elliot, J. L., Dunham, E., and Mink, D. (1977). Nature **267**, 328.

Elliot, J. L., Dunham, E., Wasserman, L. H., Millis, R. L., and Churms, J. (1978). Astron. J. **83**, 980.

Elliot, J. L., French, R. G., Frogel, J. A. Elias, J. H., Mink, D. J., and Liller, W. (1981). Astron. J. **86**, 444.

Elliot, J. L., and Nicholson, P. D. (1984). "The Rings of Uranus," in *Planetary Rings*, edited by A. Brahic and R. Greenberg (University of Arizona, Tucson) (in press).

Elliot, J. L., Rages, K., and Veverka, J. (1976). Astrophys. J. **207**, 994.

Elliot, J. L., *et al.* (1984). In preparation.

Esposito, L. W., Borderies, N., Goldreich, P., Cuzzi, J. N., Holberg, J. B., Lane, A. L., Pomphrey, R. B., Terrile, R. J., Lissauer, J. J., Marouf, E. A., and Tyler, G. L. (1983). Science **222**, 57.

Frogel, J. A., and Elias, J. H. (1980). *CTIO Facilities Manual*, revised edition. (CTIO, La Serena, Chile).

Freedman, A., Tremaine, S. D., and Elliot, J. L. (1983). Astron. J. **88**, 1053.

French, R. G., *et al.* (1984). In preparation.

French, R. G., Elliot, J. L., and Allen, D. A. (1982). Nature **298**, 827.

French, R. G., and Lovelace, R. V. E. (1983). Icarus **56**, 122.

Goldreich, P., and Tremaine, S. (1979). Nature **277**, 97.

Goldreich, P., and Tremaine, S. (1982). Annu. Rev. Astron. Astrophys. **20**, 249.

Klemola, A. R., Mink, D. J., and Elliot, J. L. (1981). Astron. J. **86**, 138.

Lotsch, H., and Gray, M. (1964). Commun. ACM **1**, 660.

Marouf, E. A., Tyler, G. L., Zebker, H. A., Simpson, R. A., and Eshleman, V. R. (1983). Icarus **54**, 189.

Nicholson, P. D., Matthews, K., and Goldreich, P. (1982). Astron. J. **87**, 433.

Nicholson, P. D., Persson, S. E., Matthews, K., Goldreich, P., and Neugebauer, G. (1978). Astron. J. **83**, 1240.

Pang, K. D., and Nicholson, P. D. (1984). *Proceedings of the Fifteenth Lunar and Planetary Science Conference* (Pergamon, New York) (in press).

Peterson, D. M. (1979). "Lunar Occultations: Working Notes," private circulation.

Ridgway, S. T., Joyce, R. R., White, N. W., and Wing, R. F. (1980). Astrophys. J. **235**, 126.

Rossi, B. B. (1959). *Optics* (Addison-Wesley, Reading, Mass.), p. 191.

Smart, W. M. (1977). *Textbook on Spherical Astronomy* (Cambridge University, Cambridge, England), p. 368.

Smith, B. A., *et al.* (1982). Science **215**, 504.

Tyler, G. L., Marouf, E. A., Simpson, R. A., Zebker, H. A., and Eshleman, V. R. (1983). Icarus **54**, 160.

van de Hulst, H. C. (1957). *Light Scattering by Small Particles* (Wiley, New York; corrected edition, 1981, Dover, New York).